Economic Sciences
https://economic-sciences.com
ES(2026) | Vol. 22, No. MIC'26 | Pg:223-238 | ISSN:1505-4683

Next-Generation Tandem Photovoltaics: Role of Multinary Compound Semiconductors in Efficiency Enhancement

Dr.Aditi Sharma
Assistant professor, Prestige institute of Management and Research Bhopal.
Email id- aditii.sharma008@gmail.com

Abstract

Tandem cells offer a direct path around the spectral utilisation limit of the single-junction PV devices, by using two absorbers with complementary bandgaps to capture high- and low-energy photons. This study critically explores the numerical dataset of a SCAPS-1D perovskite model in order to investigate the potential for the multinary, lead-free perovskite absorbers for enhancing the performance of two terminal monolithic tandem perovskite solar cells. The top absorber of two double perovskite designs was either a narrow-bandgap crystalline-silicon heterojunction bottom cell with a 1.3-eV bandgap ($CsSnI_3$) or a wide-bandgap quaternary-substituted double perovskite with a bandgap of ~1.8 eV. The model is solved for one dimensional Poisson, carrier-continuity and drift-diffusion equations, in AM1.5G illumination at 300K. SCAPS-1D is not capable of solving a full multijunction device, so the sub-cells were calibrated separately, the spectrum transmitted through the top stack was calculated and the absorber thicknesses were swept so that the two sub-cells were close to a common short-circuit current. The perovskite/silicon design has been optimized to achieve JSC = 0.181068 mA $cm^{-}2$ @ 550 nm (top-absorber) and VOC = 0.1812 V @ 230 µm (bottom-absorber), resulting in a FF of 0.7918 and a PCE of 0.2595. The all-perovskite design reached its optimum at 700 nm and 65 nm, respectively, with JSC = 16.91 mA cm^{-2}, VOC = 1.73 V, FF = 83.72% and PCE = 24.47%. The tandem configuration achieved a 19.81% and 50.12% improvement in PCE compared to the best stand-alone bottom-cell efficiencies analyzed, for the Si-based and all-perovskite systems, respectively. The results demonstrate the usefulness of multinary composition control for the elimination of lead and bandgap allocation, voltage addition and/or spectral complementarity. Principal unresolved issues include losses due to optical reflection, recombination-junction modelling, migration of ions, long term stability and experimental manufacturability.

Keywords: *tandem photovoltaics; multinary semiconductors; lead-free perovskites; Cs2AgBi0.75Sb0.25Br6; CsSnI3; perovskite/silicon; current matching; SCAPS-1D; efficiency enhancement*

1. Introduction

The PV power conversion relation between the incident solar spectrum and electronic band structure of the absorber is the fundamental control of PV power conversion. The photons with energy below the bandgap are transmitted while the energy of photons that are significantly higher than the bandgap of the cell is mostly lost through thermalisation of the carriers. The detailed-balance analysis of Shockley and Queisser therefore sets a practical limit on the efficiency of an ideal single absorber, and the tandem extension developed by Alexis De Vos demonstrates that this limit can be increased by stacking absorbers with different bandgaps [1,2].

Two terminal monolithic tandem cells are especially desirable since the sub-cells are optically stacked and electrically in series. The voltage of them add up, the currents through them are the same. Consequently, tandem optimisation is not an easy task of finding the highest performing cell in the top or the bottom row separately. This is a coupled design challenge that involves interacting with main design components such as bandgap, thickness, absorption coefficient, transport layers, defect density, recombination contacts and parasitic losses all influencing the current-matching point. In recent years, perovskite/silicon research has shown that the optimization of interfaces, texture engineering, and optical coupling and scalable fabrication is as critical as the quality of the absorbers [4–12].

The use of chemical substitution allows for a much broader compositional design space for multinary compound semiconductors to be used in this coupled optimisation process than for elemental

Economic Sciences
https://economic-sciences.com
ES(2026) | Vol. 22, No. MIC'26 | Pg:223-238 | ISSN:1505-4683

and binary absorbers. The category contains chalcopyrite compounds (Cu(In,Ga)Se2), kesterite compounds (Cu2ZnSn(S,Se)4), chalcogenide perovskites and complex halide perovskites. They affect the constituent ratios which can alter bandgap, defect chemistry, electron affinity, lattice strain, phase stability and carrier transport. In tandem devices, this tunability can be exploited to make the front sub-cell a material with a wide bandgap, and the rear sub-cell a material with a narrow bandgap, thus maximizing the spectral coverage and maintaining a high total voltage [20–25].

In the present numerical study, two multi-nary halide absorbers consisting of lead (Pb) with either selenium (Se) or tellurium (Te) are studied. A compositionally substituted double perovskite viz Cs2AgBi0.75Sb0.25Br6 is utilized as the ~1.8 eV top absorber. It has more than binary B-site chemistry which is relevant to lead-free band gap and defect engineering. In the all-perovskite construction, the rear absorber is approximately 1.3 eV CsSnI3, which is a strong absorber of near-infrared photons and sensitive to defect and Sn2+ oxidation that causes self-doping issues [15–20]. The tandem is made up of two types of cells: a double-perovskite top cell and a crystalline silicon heterojunction bottom cell. The second uses CsSnI3 to replace silicon, which results in a configuration with two lead-free absorbers, all perovskite, 3-3-3.The second one uses CsSnI3 to replace silicon to form an all perovskite configuration with two lead-free absorbers, 3-3-3.

The study aims at achieving four objectives as follows:

(i) develop a repeatable numerical protocol based on the SCAPS-1D computer simulation;

(iii) to measure the current matching requirements of the two tandem designs proposed; and

(iii) to describe the simulated improvements for efficiency in terms of spectral allocation, voltage addition and absorber thickness;

(iv) to recognize possible assumptions and constraints which must be dealt with prior to experimental translation.

The contribution is not an experimentally fabricated claim. Rather it offers the analysis and internal checks of a numerical set, with a review of recent papers as a benchmark and clear identification and correction of known inconsistent points in the transcription.

2. Multinary Semiconductors in Tandem Photovoltaics

2.1 Bandgap allocation and series-current constraint

In the case of the 2T tandem, it is desired that the front absorber transmit enough photons that cannot be efficiently converted in the WG sub-cell, but that it absorb a sufficient number of visible photons to contribute a similar current as does the rear cell. If the two cells are connected in series, the short circuit current of the combination is controlled by the lower value of the short circuit current of the two cells, while the open circuit voltage is close to the sum of the two. This generates a tradeoff between top-cell thickness, which increases the top-cell absorption and current, but decreases the amount of photons that can be sent to the bottom cell. When both thickness-dependent current curves intersect near the maximum current, the optimum current is located near the intersection of the two curves, not the same as the maximum current for either a single thickness thick current curve individually.

2.2 Why multinary absorbers are useful

Absorbers using the same material in more than one form (as for different applications) can be used in tandem design by tuning Ee and Gap of the composition. The bandgap in CIGS can be varied by changing the ratio of In to Ga at a given site, the absorption edge in CZTSSe can be changed by varying the S/Se ratio, and cation and anion substitution in chalcogenide perovskites changes both the bandgap and stability, whereas the ratio of mixed cations, mixed halides or mixed metal sites in halide perovskites allows wide- and narrow-bandgap formulations. These recent searches based on data have also extended the envisioned chalcogenide design space, but compounds must also be selected to be defect tolerant, abundant in

Economic Sciences
https://economic-sciences.com
ES(2026) | Vol. 22, No. MIC'26 | Pg:223-238 | ISSN:1505-4683

elements, and free from toxicity and phase impurities and be scalable for deposition.

Multinary double perovskites are realized by previously discussed partial substitution of Bi by Sb in Cs2AgBi1−xSbxBr6 for the top-cell material discussed herein. This composition does not contain a lead and gives a high voltage contribution to the unit, but can have an indirect transition, deep defect and carrier mobility which is relatively low, so that the current is limited. CsSnI3 is better for long wavelength absorption and has a lower bandgap, but requires the suppression of Sn vacancies, oxidation and the related non-radiative recombination for the bottom perovskite. The tandem design therefore capitalizes upon the synergistic abilities of both absorber families whilst also incorporating the weaknesses.

2.3 Research gap

Most of the high efficiency experimental tandem devices are based on mixed-halide perovskites containing lead on silicon or narrow-bandgap perovskites containing tin/lead in all perovskite structures. Most research on lead-free double perovskites has been used to look at them as single cells, or as a preliminary example. In contrast, there has been comparatively little work to evaluate the Cs2AgBi0.75Sb0.25Br6 top absorber coupled with a CsSnI3 bottom absorber under the same filtered-spectrum and current-matching conditions. The paired analysis here gives a controlled comparison of the performance of a fixed wide-bandgap multinary absorber in combination with an already proven silicon rear cell, and a compositionally tunable lead-free perovskite rear cell.

3. Numerical Methodology

3.1 Study design and data provenance

In this paper a numerical device-simulation method is used based on SCAPS-1D modelling of two PV architectures with two terminals. The simulation records that were available were all governing electrical equations, material parameters, defect models, contact settings, optical filtering procedure and the final outputs of the photovoltaics themselves, as well as sweeps of the thickness of the absorbers. All these inputs and outputs were compared and sorted into a single, analytically coherent flow and analyzed by applying the concise correlation between short-circuit current density, open-circuit voltage, fill factor and power-conversion efficiency. No experimental measurements were not reported that were added to the analysis.

The numerical investigation was carried out in the following four steps. The calibration of the standalone Top and Bottom sub-cells was done independently. Secondly, the AM1.5G spectrum was sent through the top-cell stack with changing thicknesses of the top-absorbers. Third, the filtered spectrum was simulated for each bottom cell. Finally, the thicknesses of the absorbers have been changed to find the value where, the short circuit current densities of the top and bottom sub-cells are the same.

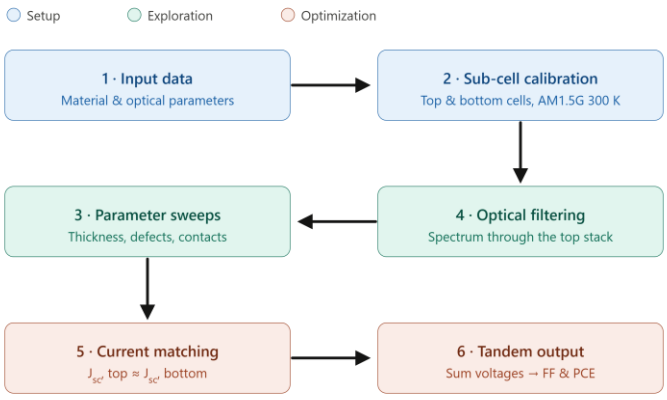

Figure 1. Numerical workflow used to calibrate, optically couple and current-match the tandem sub-cells.

Economic Sciences
https://economic-sciences.com
ES(2026) | Vol. 22, No. MIC'26 | Pg:223-238 | ISSN:1505-4683

3.2 SCAPS-1D device model

One-dimensional semiconductor simulator SCAPS-1D version 3.3.09 was used. It was initially created to analyze thin-film solar-cells and allows definition of multiple layers, bulk defects, interface defects as well as optical absorption files, front and rear contacts, series and shunt resistances, batch parameter sweeps and computation of J–V, C–V, C–f and quantum-efficiency characteristics [3]. Lateral uniformity of the properties was assumed in each sub-cell, representing it as an unidimensional stack. The electrical solution comprises of electrostatics and carrier conservation and drift-diffusion transport.

$$d/dx\ [\ \varepsilon_0\ \varepsilon_r\ d\psi/dx\ ] = -q\ (p - n + N_D^+ - N_A^- + p_t - n_t) \quad (1)$$

$$\partial n/\partial t = (1/q)\ \partial J_n/\partial x + G - U_n\ ; \quad \partial p/\partial t = -(1/q)\ \partial J_p/\partial x + G - U_p \quad (2)$$

$$J_n = q\ \mu_n\ n\ E + q\ D_n\ dn/dx\ ; \quad J_p = q\ \mu_p\ p\ E - q\ D_p\ dp/dx \quad (3)$$

ψ is electrostatic potential, n and p are free-electron and hole concentrations, ND and NA are the concentrations of ionised donors and acceptors, respectively, nt and pt are the concentrations of trapped carriers, respectively, Jn and Jp are current densities of free electrons and free holes, respectively, μ and D are the free-electron and free hole mobility, respectively, and G is the photogeneration and U is the net recombination rate. The defect distributions were considered in SCAPS as bulk and interface defects, and recombination could adjust to the density of defects, energy level and capture cross section of defects.

3.3 Optical filtering and tandem reconstruction

The incident power density of AM1.5G spectrum was 1000 W m−2 and at the temperature of 300K in the top cell. The incident spectrum was attenuated by the top stack to obtain the spectrum delivered to the bottom cell. In this provided implementation, the intermediate reflection loss has been ignored, coherent interference and scattering loss is also ignored and only front contact transmission is taken into account in the input spectrum. The transmitted spectrum of a stack with i optical layers was given as:

$$S(\lambda) = S_0(\lambda)\ \exp\ [\ -\Sigma_i\ \alpha_i(\lambda)\ d_i\ ] \quad (4)$$

where S0(λ) is the incident AM1.5G spectrum, αi(λ) is the wavelength-dependent absorption coefficient and di is the thickness of layer i. The top and bottom cells were solved separately in SCAPS-1D since it does not calculate a complete two-terminal multijunction stack. The top-cell J-V curve presents the results from an AM1.5G spectrum, while the bottom-cell curve presents a calculation under each corresponding filtered AM1.5G spectrum. The tandem voltage Vtandem (J) was recovered under a standard current J, where Vtandem (J) = Vtop (J) + Vbottom (J). To make the current matching condition, the absorber thickness is adjusted and the maximum common JSC is found.

$$FF = (V_{mp}\ J_{mp})/(Voc\ Jsc)\ ; \quad PCE\ (\%) = Voc\ Jsc\ FF\ /\ P_{in} \quad (5)$$

Economic Sciences
https://economic-sciences.com
ES(2026) | Vol. 22, No. MIC'26 | Pg:223-238 | ISSN:1505-4683

3.4 Device architectures

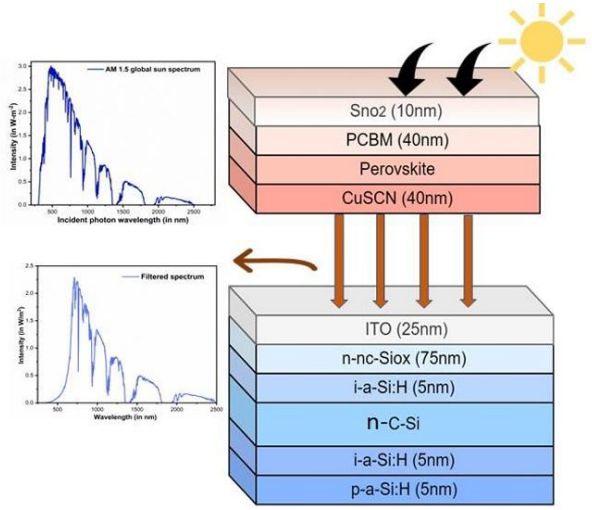

(a)

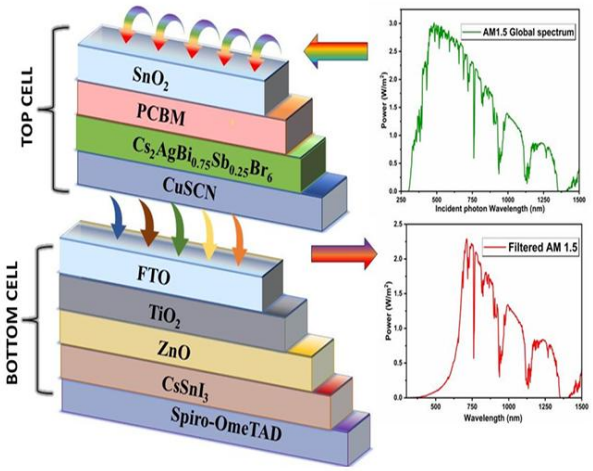

(b)

Figure 2. Reconstructed layer sequences of the two simulated two-terminal tandem architectures. Thicknesses correspond to the selected current-matched designs

Table 1. Layer sequences and functional roles of the investigated tandem cells.

Architecture	Top sub-cell	Bottom sub-cell	Electrical/optical role
Tandem 1	SnO2 / PCBM / Cs2AgBi0.75Sb0.25Br6 / CuSCN	ITO / n-nc-SiOx / i-a-Si:H / n-c-Si / i-a-Si:H / p-a-Si:H	Wide-bandgap visible absorption coupled to a high-quality near-infrared silicon heterojunction
Tandem 2	SnO2 / PCBM / Cs2AgBi0.75Sb0.25Br6 / CuSCN	FTO / TiO2-ZnO / CsSnI3 / Spiro-OMeTAD	Fully perovskite spectral division using approximately 1.8 eV and 1.3 eV lead-free absorbers

3.5 Silicon bottom-cell material parameters

The bottom cell consisted of an n-type crystalline-silicon wafer sandwiched in between intrinsic and doped amorphous-silicon passivation and contact layers, respectively, for the silicon heterojunction bottom cell. Table 2 gives an overview of the key materials used in the source data set. During the tandem matching, the silicon thickness was changed, but the single silicon thickness was reported as 150 µm and the optimal tandem thickness as 230 µm. Changes in the preliminary result would be recorded in an earlier descriptive statement as a preliminary design value.

Economic Sciences
https://economic-sciences.com
ES(2026) | Vol. 22, No. MIC'26 | Pg:223-238 | ISSN:1505-4683

Table 2. Electrical parameters used for the silicon heterojunction bottom cell.

Parameter	ITO	n-nc-SiOx	i-a-Si:H	n-c-Si	p-a-Si:H
Thickness	25 nm	75 nm	5 nm	Variable	5 nm
Bandgap Eg (eV)	3.72	1.40	1.72	1.12	1.72
Electron affinity χ (eV)	3.60	3.94	3.80	4.05	3.80
Relative permittivity εr	9.4	11.9	11.9	11.9	11.9
Nc (cm−3)	2.2×10^{19}	2.8×10^{19}	2.5×10^{20}	2.8×10^{19}	2.5×10^{20}
Nv (cm−3)	1.8×10^{19}	1.4×10^{19}	2.5×10^{20}	1.04×10^{19}	2.5×10^{20}
Electron mobility (cm² V−1 s−1)	10	1.4×10^{3}	20	1.4×10^{3}	20
Hole mobility (cm² V−1 s−1)	10	4.5×10^{2}	5	4.5×10^{2}	5
Donor density ND (cm−3)	1×10^{19}	1×10^{20}	0	5×10^{16}	0
Acceptor density NA (cm−3)	—	—	0	—	1×10^{20}

Tandem current matching was a procedure used to change Si thickness. Stand alone calibration was done with the silicon thickness of 150 µm while the optimum tandem calibration was found to be 230 µm. A preliminary value of 250µm was found in the design record, and is assumed to be an initial design configuration, and not the current matched thickness.

3.6 Defects, contacts and sweep conditions

Cs2AgBi0.75Sb0.25Br6 absorber was given a bulk defect density of 2.5 × 1013 cm−3, a Gaussian distribution of defects and a characteristic energy of 0.1 eV. The silicon heterojunction contained intrinsic a-Si:H with amphoteric Gaussian defects and band-tail states, while the doped a-Si:H layers has lower densities of amphoteric defects and band-tail states were present. Single-level centres (neutral defects) were used to represent interface defects. The Tandem 2 was assumed to have flat-band contacts. The 107 and 105 cm s−1 surface recombination velocities for electrons and holes were at the front contact and the carrier selectivity was inverted at the back contact.

Table 3. Simulation conditions and thickness sweeps used for tandem optimisation.

Model element	Tandem 1 setting	Tandem 2 setting	Purpose
Illumination	AM1.5G, 1000 W m−2, 300 K	AM1.5G, 1000 W m−2, 300 K	Standardised input and direct comparison
Top absorber sweep	Approximately 80–700 nm; selected 550 nm	100–900/1000 nm; selected 700 nm	Control top-cell absorption and transmitted flux
Bottom absorber sweep	c-Si approximately 50–300 µm; selected 230 µm	CsSnI3 approximately 50–350 nm; selected 65 nm	Locate the common-current intersection
Top absorber defects	2.5×10^{13} cm−3, Gaussian, 0.1 eV	Same wide-bandgap absorber model	Account for non-radiative recombination
Optical coupling	23 filtered-spectrum files reported	Thickness-specific filtered spectra	Provide bottom-cell illumination
Tandem connection	Series reconstruction at matched JSC	Series reconstruction at matched JSC	Add voltages while enforcing one current

3.7 Validation and internal consistency checks

The validation and internal consistency checks are included. A standalone sub-cell was calibrated prior to optical and electrical tandem reconstruction to experimentally reported or previously reported benchmark cell behaviour. For each of the efficiencies reported, the equation 5 was used to confirm it. This test of arithmetic found three definite discrepancies on the numbers available from the records of the simulated experiments. The first is that Tandem 1's filtered-spectrum silicon voltage should not be 7044 V, but instead 0.7044 V. The second one is not possible for a single silicon sub-cell and is not consistent with the tandem voltage.

Economic Sciences
https://economic-sciences.com
ES(2026) | Vol. 22, No. MIC'26 | Pg:223-238 | ISSN:1505-4683

Second, the standalone $CsSnI_3$ voltage is about 0.704 V (not 0.073 V) when taking into account the JSC = 33.31 mA cm^{-2}, VOC ≈ 0.704 V and FF = 69.5%, which is consistent with the reported standalone efficiency. Third, the current-matching calculation and performance table show 550 nm as the thickness selected for the top-absorber in Tandem 1 while one summary record states 500 nm. Thickness-dependent current intersection and final output parameters are taken as being 550 nm, as it is the value that corresponds to the above mentioned parameters. The above corrections have no impact on the relative findings of the study. They enhance the numerical consistency and provide control of the reported current, voltage, fill factor and efficiency that fulfill the governing photovoltaic relations.

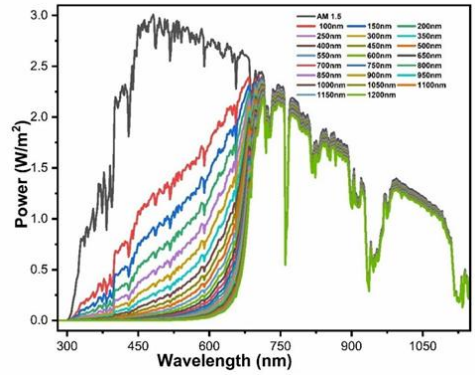

Figure 3: Filtered spectra with the original AM1.5G spectrum.

Figure 3. Current matching map as a function of the thickness of the absorber in Tandem 1, reconstructed from the set of thickness sweep of the absorbers. The design chosen consists of a 550 nm $Cs_2AgBi_{0.75}Sb_{0.25}Br_6$ top absorber and a 230 µm crystalline-silicon bottom absorber.

4. Results

4.1 Standalone sub-cell calibration

The calibrated wide-bandgap top cell achieved an efficiency of about 14.3% PCE in both tandem structures. For Tandem 1, the reported top-cell condition corresponding to the selected 550 nm absorber gave JSC = 18.1068 mA cm−2, VOC = 1.12 V, FF = 74.15% and PCE = 14.85%. The standalone silicon heterojunction reached JSC = 36.152 mA cm−2, VOC = 0.731 V, FF = 81.93% and PCE = 21.66% at a reported calibrated thickness of 150 µm. The silicon current is much greater due to its lower silicon bandgap of 1.12 eV and wide NIR range of response.

For Tandem 2, the wide-bandgap top cell under AM1.5G generated JSC = 16.92 mA cm−2, VOC = 1.137 V, FF = 74.539% and PCE = 14.33%. The standalone CsSnI3 cell generated JSC = 33.31 mA cm−2, a corrected VOC of approximately 0.704 V, FF = 69.5% and PCE = 16.30%. These baselines show the expected asymmetry between the two cells: the wide bandgap has high voltage and low current, the narrow bandgap has high current under the un-filtered spectrum.

Table 4. Standalone performance used to establish the tandem baselines.

Sub-cell / condition	JSC (mA cm−2)	VOC (V)	FF (%)	PCE (%)	Interpretation
T1 wide-gap top, selected thickness	18.1068	1.120	74.15	14.85	Current-limiting under standalone AM1.5G
Silicon bottom, standalone calibration	36.152	0.731	81.93	21.66	High-current near-infrared bottom cell
T2 wide-gap top, standalone	16.92	1.137	74.539	14.33	High-voltage top absorber
CsSnI3 bottom, standalone	33.31	≈0.704	69.50	16.30	Corrected voltage from PCE identity

Economic Sciences
https://economic-sciences.com
ES(2026) | Vol. 22, No. MIC'26 | Pg:223-238 | ISSN:1505-4683

4.2 Tandem 1: Cs2AgBi0.75Sb0.25Br6/silicon

The photocurrent of the double-perovskite top absorber was increased while the irradiance reaching the silicon bottom cell was decreased as its thickness was increased. Optical calculations resulted in 23 thickness dependent filtered spectra which were applied to silicon absorbers ranging about 50–300 µm in thicknesses. Several crossings of the upward trend of top-cell current and the downward family of silicon bottom-cell current were seen. The best common current was found at 550 nm top absorber and 230 µm Si wafer.

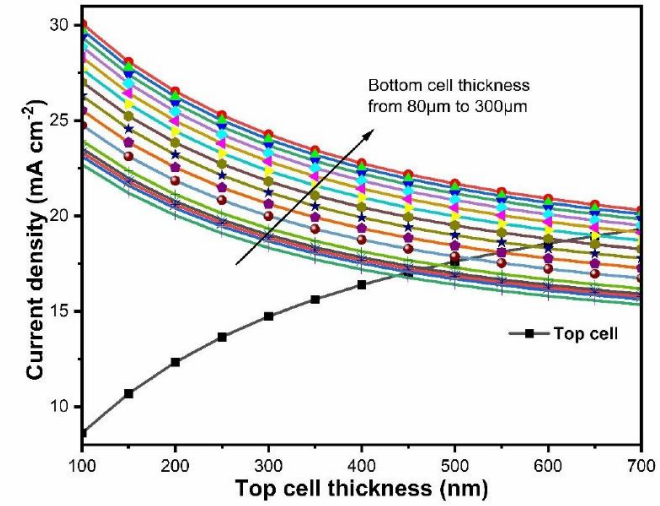

Figure 4: At thicknesses ranging from 50 to 700 nm for the top absorber layer, this curve was employed to establish current matching conditions for both the top and bottom cells.

Figure 4. Current-matching map for Tandem 2 as a function of the absorber thickness (reconstructed from the data available in the absorber-thickness sweep). The design selected has a 700nm $Cs_2AgBi_{0.75}Sb_{0.25}Br_6$ absorber on top and a 65nm $CsSnI_3$ absorber on bottom.

Table 5. Current-matched photovoltaic parameters of Tandem 1.

Component / operating condition	Thickness	JSC (mA cm−2)	VOC (V)	FF (%)	PCE (%)
Wide-bandgap top under AM1.5G	550 nm	18.1068	1.120	74.15	14.85
Silicon bottom under filtered spectrum	230 µm	18.085	0.7044	82.97	18.55
Reconstructed 2T tandem	550 nm / 230 µm	18.1068	1.812	79.18	25.95

The tandem efficiency is 19.81% better than the silicon tandem efficiency used for calibration, or 4.29 absolute percentage points (APPs) higher. The main source of the gain is from voltage addition where the tandem current is more or less half the standalone silicon current, and the operating voltage is more or less 2.48 times the standalone silicon VOC. The diagram shows the central tandem principle: the efficiency can be achieved without retaining the entire current of the low-bandgap cell, as long as the ratio between the currents allocated by the spectrally allocated sub-cells is sufficiently high and the voltage losses of both sub-cells are kept under control.

4.3 Tandem 2: Cs2AgBi0.75Sb0.25Br6/CsSnI3

The thickness of the $Cs_2AgBi_{0.75}Sb_{0.25}Br_6$ top-absorber was varied from about 100 nm to 900-1000 nm for the all-perovskite tandem. The thickness of the $CsSnI_3$ bottom-absorber was changed from about 50 nm to 350 nm corresponding to each filtered spectrum. As the 'top

Economic Sciences
https://economic-sciences.com
ES(2026) | Vol. 22, No. MIC'26 | Pg:223-238 | ISSN:1505-4683

absorber' got thicker the 'current' coming to it began to move towards a saturation region, while the 'photon flux' and 'current' available to the 'bottom cell' decreased. A top absorber with 700 nm thickness and a bottom absorber with 65 nm thickness were used to obtain the desired current matching region.

Under the respective illumination conditions (15.57 mW cm−2 and 15.51 mW cm−2), current densities of 16.81 mA cm−2 and 17.10 mA cm−2 were reported for the top and bottom cells, respectively, and 16.91 mA cm−2 was assigned to the reconstructed tandem. This is about 1.7% mismatch and more than the mismatch found at Tandem 1, and is considered to be a finite-step, rounding/transcription uncertainty, not a strict equality. However, the chosen family-thickness cross-point is in the crossing area of the two existing families. Based on Equation 5, the reported tandem VOC of 1.73 V and the FF of 83.72% and the PCE of 24.47% are consistent with each other.

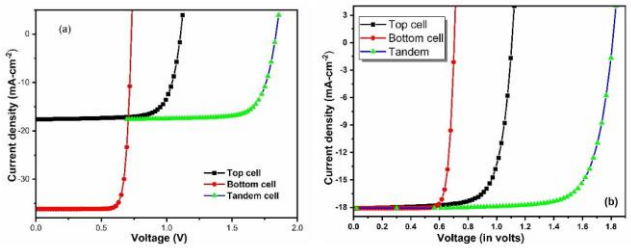

Figure 5: (a) Standalone J-V curves for the top, bottom, and tandem cells (b) J-V curves at the point of current matching.

The respective illumination conditions of the top cell and the bottom cell in the source table give values of 16.81 mA/ cm2 and 17.10 mA/ cm2, respectively, and the value 16.91 mA/ cm2 is assigned to the tandem cells reconstructed. This 1.7% spread is greater than the mismatch of the 'Tandem 1' and so should be considered as a rounding or transcription error not a match. However, this selected region is definitely the crossing region of the two existing families. The reported tandem VOC of 1.73V, FF of 83.72% and PCE of 24.47% are consistent for each other, according to Equation 5.

Table 6. Current-matched photovoltaic parameters of Tandem 2.

Component / operating condition	**Thickness**	**JSC (mA cm−2)**	**VOC (V)**	**FF (%)**	**PCE (%)**
Wide-bandgap top under AM1.5G	700 nm	16.81	1.137	74.54	14.33
CsSnI3 bottom under filtered spectrum	65 nm	17.10	0.600	73.77	13.89
Reconstructed 2T tandem	700 nm / 65 nm	16.91	1.730	83.72	24.47

The tandem efficiency is 8.17 absolute percentage points (~ 50.12% in relative value) higher than the standalone CsSnI3 efficiency. The higher percentage increase compared to Tandem 1 is due to the lower voltage and fill factor of the stand-alone narrow-bandgap perovskite than the calibrated silicon cell. The all-perovskite tandem is thus favourably impacted by the 1.137 V contribution of the top-cell, but the extremely thin 65 nm CsSnI3 absorber and the more streamlined interconnection are experimental items that will need to be tested.

Economic Sciences
https://economic-sciences.com
ES(2026) | Vol. 22, No. MIC'26 | Pg:223-238 | ISSN:1505-4683

4.4 Comparative performance

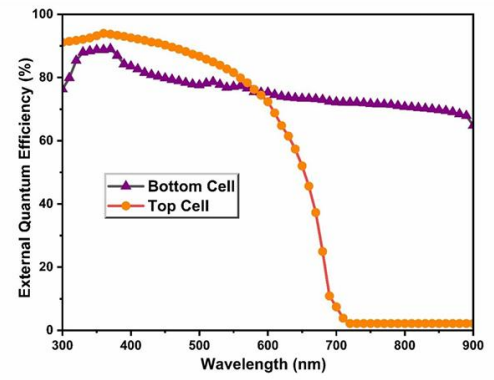

Figure 6. Efficiency of the standalone sub-cells and the corresponding tandem configurations in the supplied numerical dataset.

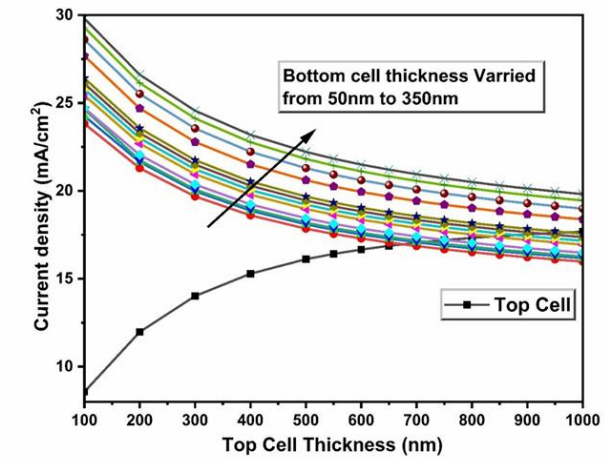

Figure 7. Comparison of the reported current-matched tandem metrics; bar heights are normalized within each metric and labels show the original values.

Table 7. Comparative interpretation of the two tandem architectures.

Comparison metric	Tandem 1: perovskite/silicon	Tandem 2: all-perovskite	Analytical implication
Top / bottom bandgap	1.8 / 1.12 eV	1.8 / 1.3 eV	Silicon provides broader near-infrared coverage
Matched JSC	18.1068 mA cm−2	16.91 mA cm−2	Tandem 1 retains the larger common current
Tandem VOC	1.812 V	1.73 V	Tandem 1 has the higher combined voltage
Fill factor	79.18%	83.72%	Tandem 2 reports the squarer reconstructed J–V curve
PCE	25.95%	24.47%	Tandem 1 leads by 1.48 percentage points
Relative PCE gain vs best standalone bottom	19.81%	50.12%	Tandem 2 derives the larger proportional benefit
Principal practical	Thick, high-quality silicon and	Sn oxidation,	Different scale-up constraints

Economic Sciences
https://economic-sciences.com
ES(2026) | Vol. 22, No. MIC'26 | Pg:223-238 | ISSN:1505-4683

risk	interconnection losses	ultrathin absorber control and all-perovskite stability	despite similar simulated PCE

5. Discussion

5.1 Efficiency enhancement mechanism

From the results shown, you can see three different functions of the multinary top absorber. First, it absorbs a significant portion of high energy photons from the incident beam and absorbs the lower energy photons at a higher voltage than the bottom cell. Second, because of its finite thickness, it functions as an optical filter that dictates the current that is available to the back absorber. Third, due to its multinary composition, it provides a pathway to bandgap and defect tuning without lead. This theoretical optimum thickness is thus an electro-optical rather than an absorptive maximum thickness.

The higher PCE value of Tandem 1 is attributed to the silicon material which has a well-developed heterojunction contact system, good long-wavelength collection, and a high standalone fill factor. In the selected 230 µm wafer, the current under filtered-spectrum is kept around 18.1 mA/cm2 and the additional voltage added to the top cell is about 0.70 V. Tandem 2 uses a lower matched current and voltage, but it's matched FF is higher than that of the other units, so it makes up for that loss. The all-perovskite architecture also provides for a thinner active stack and can also be processed at lower temperatures, although this is not assumed from a one-dimensional electrical model.

5.2 Position relative to recent tandem literature

The simulated efficiencies of 25.95% and 24.47% are reasonable but show efficiencies that are less than those of a few recent experimental devices that include perovskite/silicon combinations as cited in reviews and primary publications. The fully textured and nanotextured monolithic devices have been proven to allow optical management and interface quality to bring perovskite/silicon tandems from the mid 20% to surpass the 30% limit [7–12]. According to a 2026 review, the wider technology is at about 34.85% commercial readiness and durability, module integration and manufacturing cost are the remaining commercial barriers [6]. This new Tandem 1 result should thus be seen as a learning study of the absorber case, not as a record.

To date, experimental device and module performance with all-perovskite tandem devices has been improved due to improved grain surface passivation and module processing, as well as narrow-bandgap absorber control [13,14]. In recent years, SCAPS-1D calculations have shown efficiencies greater than 30% for materials with low amount of lead and alternative vacancy ordered perovskites [21]. That 24.47% corresponds to results from this paper, which are below results from best case simulations, yet has the benefit of being two of the reported absorber compositions that are lead-free. The value of the silicon-coupled version of the same WBP Top Absorber is therefore in the direct comparison with this.

Table 8. Contextual benchmark against selected tandem studies. Values are compared as reported and are not directly equivalent across area, certification and test protocol.

Study / year	Architecture	Type	Reported PCE	Relevance to the present results
Florent Sahli and co-authors, 2018 [7]	Perovskite/silicon, fully textured	Experimental, certified steady state	25.2%	Comparable to Tandem 1; demonstrates texture-enabled optical gain
Philipp Tockhorn and co-authors, 2022 [8]	Perovskite/silicon, nanotextured	Experimental, certified	29.80%	Shows the importance of optical texture and rear reflectors
Jiang Liu and co-	Perovskite/silicon	Experimental	>33%	Highlights interface

Economic Sciences
https://economic-sciences.com
ES(2026) | Vol. 22, No. MIC'26 | Pg:223-238 | ISSN:1505-4683

authors, 2024; reviewed in [4–6]	with bilayer passivation		class	passivation beyond the present simplified model
Renxing Lin and co-authors, 2022 [13]	All-perovskite tandem	Experimental	High-20% class	Demonstrates grain-surface passivation for all-perovskite tandems
Xuezeng Dai and co-authors, 2022 [14]	All-perovskite tandem module	Experimental module	>20% class	Addresses cell-to-module derating absent from SCAPS
Navdeep Kaur and co-authors, 2025 [21]	All-inorganic low-lead/lead-free simulated tandem	SCAPS-1D	31.93%	Recent simulation benchmark with different absorber chemistry
Present Tandem 1	Lead-free double-perovskite/silicon	SCAPS-1D	25.95%	Higher of the two supplied architectures
Present Tandem 2	Lead-free all-perovskite	SCAPS-1D	24.47%	Fully lead-free absorber pair

5.3 Interpretation of the multinary-material role

The findings suggest a larger take (apart from replacing toxic or rare elements): The potential of multinary semiconductors is not just in replacing other elements in tandem photovoltaics. Composition (A Design Variable): It is a variable that relates materials chemistry to device-level spectral management. In the high energy absorber, such as Bi/Sb substitution, the electronic structure changes and consequently the gap value is approximately 1.8 eV which is suitable for high energy photon conversion. The lower gap provided by the tin iodide framework will enable the bottom absorber to collect near infrared. Similar composition–bandgap concepts are employed in mixed-halide perovskites and CIGS and CZTSSe, but each class of material has different defect and phase-stability limitations [20,22–25].

The comparison also shows that not all the limitations can be overcome with the tunable absorber. VOC can be increased by a high bandgap, while low mobility and indirect transition will reduce the current and fill factor. A low band gap can increase the spectral coverage, while high self-doping and deep recombination centres can restrict the voltage. Thus, composition, phase purity, interfaces and optical thickness needs to be managed simultaneously to be successful with tandem optimisation. In the present model, the thickness and the size of the defect are only poorly described and the model cannot solve the problem of phase segregation or ion motion depending on the composition.

5.4 Model limitations and uncertainty

The major constraint is the sequential sub-cell method. It is helpful for two terminal tandem analysis, but does not solve the recombination junction, interlayer band bending, tunnel transport and luminescent coupling in one coupled domain explicitly. When there is information from interconnection resistive or recombination loss, the voltage-addition procedure may overestimate the performance. Similarly, Equation 4 fails to consider front surface reflections, multiple reflections within the medium, coherent interference, texture-dependent scattering and angle-dependent absorption. For silicon tandems, the condition of light trapping and parasitic absorption in the transparent contacts is significant for current matching and the above mentioned omissions are particularly relevant in this context.

The calculation of the SCAPS is a one-dimensional model and assumes that each layer is laterally uniform. It cannot accommodate pinholes, networks of grain-boundaries, rough interfaces, local shunts, or inadequate coverage and/or thickness variations. It is also not a model that includes dynamic ion migration, redistribution of halides, oxidation of Sn2+, moisture ingress, thermal cycling or mechanical stress. The reported output should therefore be viewed as an upper-bound device design screen and not as a foretaste of stabilised module output.

There are also indications of numerical uncertainty in the provided data. The top and bottom currents difference for Tandem 1 is small and the summed

Economic Sciences
https://economic-sciences.com
ES(2026) | Vol. 22, No. MIC'26 | Pg:223-238 | ISSN:1505-4683

sub-cell voltages differ from the reported tandem voltage by 12 mV. Tandem 2 has a larger spread among the top, bottom and tandem current values. The inconsistencies do not affect the qualitative ranking, but precise curve reconstruction, uncertainty propagation and independent replication would require raw output files from SCAPS.

A number of values included in the simulation records provided have some uncertainty. The top and bottom cell currents of Tandem 1 differ slightly, and the voltage at the bottom cell is 12 mV different from the reported tandem cell voltage. The range of the top-cell, bottom-cell and reconstructed tandem currents is relatively large in tandem 2. They do not change the qualitative ranking of the two architectures, but it would need to have access to the original SCAPS project files and the exported J–V data sets to be able to exactly reconstruct the curves and replicate independently.

Table 9. Data-integrity corrections and interpretation of inconsistent numerical values.

Numerical issue	Inconsistent value	Value adopted in the analysis	Basis for correction
Silicon filtered-spectrum VOC	7044 V	0.7044 V	Physically realistic value and consistency with voltage addition
Standalone $CsSnI_3$ VOC	0.073 V	≈0.704 V	Required by the reported JSC, FF and 16.30% PCE
Tandem 1 selected top thickness	500 nm in one summary record	550 nm	Current-matching curve and final output consistently identify 550 nm
Tandem 2 matched currents	16.81, 17.10 and 16.91 mA cm^{-2}	Values retained separately; 16.91 mA cm^{-2} used for the tandem	Preserves the numerical outputs while acknowledging finite mismatch
Silicon absorber thickness	250 µm preliminary value and 150 µm calibration value	230 µm in the tandem	Distinguishes preliminary design, standalone calibration and tandem optimum

A comprehensive study on SCAPS-1D analysis of multinary compound semiconductors for next generation tandem PV is presented. The wide-bandgap top cell was a $Cs_2AgBi_{0.75}Sb_{0.25}Br_6$ cell and the bottom cell was a crystalline-silicon heterojunction or narrow-bandgap $CsSnI_3$ perovskite. For each architecture the region of series-current matching was identified by thickness-specific filtered-spectrum coupling, and by absorber-thickness sweeps.

5.5 Experimental validation pathway

A credible experimental programme starts with independent films/dices. The composition and phase purity of Cs2AgBi0.75Sb0.25Br6 should be confirmed by X-ray diffraction and elemental analysis, and the absorption, photoluminescence, carrier lifetime and mobility measurements ought to confirm if the assumed optical and transport parameters are indeed realistic for the compound. Thickness-dependent top-cell devices should then be fabricated to assess the ability of the 550–700 nm film thickness range to be free of pinholes and to compensate for the current gain due to bulk recombination.

The silicon tandem should be deposited on planar and textured silicon heterojunction substrates, and sub-cells resolved EQE, EL, and calibrated tandem J-V measurements should be performed. The main difficulties associated with the all-perovskite design are the preparation of a uniform 65 nm CsSnI3 absorber, excluding oxygen from the process and device, and ensuring the low loss recombination layer can be used in both halves. Stability tests should feature maximum power point tracking, thermal exposure, humidity, and repeated lighting and post-ageing structural analysis.

6. Conclusions

The integrated SCAPS-1D study of multinary compound semiconductors application in next generation Tandem PV Devices is presented. The top cell CSFW was first combined with a crystalline-silicon heterojunction bottom cell, and then with a narrow-bandgap $CsSnI_3$ perovskite bottom cell. Each architecture's series current-

matching region was found by applying both thickness-specific filtered-spectrum coupling and absorber-thickness sweeps. The perovskite/silicon tandem achieved the highest numerical results, with JSC = 18.1068 mA cm^{-2}, VOC = 1.812 V, FF = 79.18% and PCE = 25.95% for thicknesses of the top-absorber (TA) of 550 nm and the bottom-absorber (BA) of 230 µm. The all-perovskite tandem reached JSC = 16.91 mA cm^{-2}, VOC = 1.73 V, FF = 83.72% and PCE = 24.47% using a 700 nm top absorber and a 65 nm bottom absorber. The efficiency of the silicon based tandem and all-perovskite tandem cells were 19.81% and 50.12% higher respectively when compared with the best stand-alone bottom cells. The results show that multinary semiconductors can improve the performance of the tandem in three interrelated ways: (1) the bandgap allocation, (2) the complementary utilization of the spectrum, and (3) the additive generation of voltage. The front-cell bandgap engineering feature enabled by Bi/Sb substitution in the wide-bandgap double perovskite, combined with the lower-bandgap $CsSnI_3$ absorber feature that allows for photon collection in the near-infrared region, creates a lead-free sunlight absorption pathway. This comparison also demonstrates that a multinary absorber is more effective than just nominal band gap. Optimization of carrier mobility, defect density, phase stability, and interface recombination and optical thickness must be optimised simultaneously. Technological readiness for immediate use should not be assumed from the simulated efficiencies. Sequential SCAPS-1D does not explicitly address recombination-junction transport, luminescent coupling, optical interference, texture-dependent scattering or ion migration and/or environmentally induced degradation. For future work, coupled modelling between optical and electrical parts, losses on interconnections, and experimental validation under maximum-power-point conditions, which takes into account the composition of the defects, are suggested. In this scope the two architectures studied offer a convenient template for analyzing sustainable tandem PV designs. It has been found that the results set the stage for making significant contribution to the current matching, spectral complementarity and voltage enhancement of lead-free multinary compound materials and devices and also displayed the difficulty encountered at material level and device level for realizing high efficiency tandem cells in experiment.

References

1. William Shockley and Hans J. Queisser. Detailed balance limit of efficiency of p–n junction solar cells. Journal of Applied Physics 32 (1961): 510–519. https://doi.org/10.1063/1.1736034
2. Alexis De Vos. Detailed balance limit of the efficiency of tandem solar cells. Journal of Physics D: Applied Physics 13 (1980): 839–846. https://doi.org/10.1088/0022-3727/13/5/018
3. Marc Burgelman, Peter Nollet and Stefan Degrave. Modelling polycrystalline semiconductor solar cells. Thin Solid Films 361–362 (2000): 527–532. https://doi.org/10.1016/S0040-6090(99)00825-1
4. Erkan Aydin, Thomas G. Allen, Michele De Bastiani, Arsalan Razzaq, Lujia Xu, Esma Ugur, Jiang Liu and Stefaan De Wolf. Pathways toward commercial perovskite/silicon tandem photovoltaics. Science 383 (2024): eadh3849. https://doi.org/10.1126/science.adh3849
5. Yating Shi, Joseph J. Berry and Fei Zhang. Perovskite/silicon tandem solar cells: Insights and outlooks. ACS Energy Letters 9 (2024): 1305–1330. https://doi.org/10.1021/acsenergylett.4c00172
6. Yeonji Son, Jeongin Lim, Anh Khoa Le, Beom-Soo Kim, Seulki Song and Hobeom Kim. A review of perovskite/Si tandem solar cells: Internal and external components toward high efficiency, long-term durability, and commercialization. Materials Chemistry Frontiers 10 (2026): 21–51. https://doi.org/10.1039/D5QM00637F
7. Florent Sahli, Jérémie Werner, Brett A. Kamino, Matthias Bräuninger, Raphaël Monnard, Bertrand Paviet-Salomon, Loris Barraud, Laura Ding, Juan J. Diaz Leon, Davide Sacchetto, Gianluca Cattaneo, Matthieu Despeisse, Mathieu Boccard, Sylvain Nicolay, Quentin Jeangros, Bjoern Niesen and Christophe Ballif. Fully textured monolithic perovskite/silicon tandem solar cells with 25.2% power conversion efficiency. Nature Materials 17 (2018): 820–826. https://doi.org/10.1038/s41563-018-0115-4

8. Philipp Tockhorn, Johannes Sutter, Alexandros Cruz, Philipp Wagner, Klaus Jäger, Danbi Yoo, Felix Lang, Max Grischek, Bor Li, Jinzhao Li, Oleksandra Shargaieva, Eva Unger, Amran Al-Ashouri, Eike Köhnen, Martin Stolterfoht, Dieter Neher, Rutger Schlatmann, Bernd Rech, Bernd Stannowski, Steve Albrecht and Christiane Becker. Nano-optical designs for high-efficiency monolithic perovskite–silicon tandem solar cells. Nature Nanotechnology 17 (2022): 1214–1221. https://doi.org/10.1038/s41565-022-01228-8
9. Kevin A. Bush, Axel F. Palmstrom, Zhengshan J. Yu, Mathieu Boccard, Rongrong Cheacharoen, Jonathan P. Mailoa, David P. McMeekin, Robert L. Z. Hoye, Colin D. Bailie, Tomas Leijtens, Ian Marius Peters, Maxmillian C. Minichetti, Nicholas Rolston, Rohit Prasanna, Sarah Sofia, Duncan Harwood, Wen Ma, Farhad Moghadam, Henry J. Snaith, Tonio Buonassisi, Zachary C. Holman, Stacey F. Bent and Michael D. McGehee. 23.6%-efficient monolithic perovskite/silicon tandem solar cells with improved stability. Nature Energy 2 (2017): 17009. https://doi.org/10.1038/nenergy.2017.9
10. Michele De Bastiani, Alessandro J. Mirabelli, Yi Hou, Fabrizio Gota, Erkan Aydin, Thomas G. Allen, Joel Troughton, Anand S. Subbiah, Furkan H. Isikgor, Jiang Liu, Lujia Xu, Bin Chen, Emmanuel Van Kerschaver, Derya Baran, Beatrice Fraboni, Michael F. Salvador, Ulrich W. Paetzold, Edward H. Sargent and Stefaan De Wolf. Efficient bifacial monolithic perovskite/silicon tandem solar cells via bandgap engineering. Nature Energy 6 (2021): 167–175. https://doi.org/10.1038/s41560-020-00756-8
11. Han Gao, Ke Xiao, Renxing Lin, Siyang Zhao, Wenliang Wang, Sergey Dayneko, Chenyang Duan, Chenglong Ji, Hongfei Sun, Anh Dinh Bui, Chenshuaiyu Liu, Jin Wen, Wenchi Kong, Haowen Luo, Xuntian Zheng, Zhou Liu, Hieu Nguyen, Jin Xie, Ludong Li, Makhsud I. Saidaminov and Hairen Tan. Homogeneous crystallization and buried interface passivation for perovskite tandem solar modules. Science 383 (2024): 855–859. https://doi.org/10.1126/science.adj6088
12. Yihua Chen, Ning Yang, Guanhaojie Zheng, Fengtao Pei, Wentao Zhou, Yu Zhang, Liang Li, Zijian Huang, Guilin Liu, Ruiyang Yin, Huanping Zhou, Cheng Zhu, Tinglu Song, Chun Hu, Dezhi Zheng, Yang Bai, Ye Duan, Yakuan Ye, Yiliang Wu and Qi Chen. Nuclei engineering for even halide distribution in stable perovskite/silicon tandem solar cells. Science 385 (2024): 554–560. https://doi.org/10.1126/science.ado9104
13. Renxing Lin, Jian Xu, Mingyang Wei, Yurui Wang, Zhengyuan Qin, Zhou Liu, Jinlong Wu, Ke Xiao, Bin Chen, So Min Park, Gang Chen, Harindi R. Atapattu, Kenneth R. Graham, Jun Xu and Jia Zhu. All-perovskite tandem solar cells with improved grain surface passivation. Nature 603 (2022): 73–78. https://doi.org/10.1038/s41586-021-04372-8
14. Xuezeng Dai, Shangshang Chen, Haoyang Jiao, Liang Zhao, Ke Wang, Zhenyi Ni, Zhenhua Yu, Bo Chen, Yongli Gao and Jinsong Huang. Efficient monolithic all-perovskite tandem solar modules with small cell-to-module derate. Nature Energy 7 (2022): 923–931. https://doi.org/10.1038/s41560-022-01102-w
15. Tao Ye, Ke Wang, Yuchen Hou, Dong Yang, Nicholas Smith, Brenden Magill, Jungjin Yoon, Rathsara R. H. H. Mudiyanselage, Giti A. Khodaparast, Kai Wang and Shashank Priya. Ambient-air-stable lead-free CsSnI3 solar cells with greater than 7.5% efficiency. Journal of the American Chemical Society 143 (2021): 4319–4328. https://doi.org/10.1021/jacs.0c13069
16. K. P. Marshall, Matthew Walker, Richard I. Walton and Ross A. Hatton. Enhanced stability and efficiency in hole-transport-layer-free CsSnI3 perovskite photovoltaics. Nature Energy 1 (2016): 16178. https://doi.org/10.1038/nenergy.2016.178
17. Shuo Lin, Baoping Zhang, Tie-Yu Lü, Jin-Cheng Zheng, Huaqing Pan, Huanting Chen and Chuanjin Lin. Inorganic lead-free B-γ-CsSnI3 perovskite solar cells: A numerical simulation study. ACS Omega 6 (2021): 26689–26698. https://doi.org/10.1021/acsomega.1c04096
18. Mengying Jiang and Jiyu Tang. Simulated development and optimized performance of narrow-bandgap CsSnI3-based all-inorganic perovskite solar cells. Journal of Physics D: Applied Physics 54 (2021): 465104. https://doi.org/10.1088/1361-6463/ac1e4c
19. M. Khalid Hossain, G. F. Ishraque Toki, D. P. Samajdar, Muhammad Mushtaq, M. H. K. Rubel, Rahul Pandey, Jaya Madan, Mustafa K. A. Mohammed, Md. Rasidul Islam, Md. Ferdous Rahman and H. Bencherif. Deep insights into the coupled optoelectronic and photovoltaic behavior of a lead-free CsSnI3 perovskite solar cell. ACS Omega 8 (2023):

22466–22485. https://doi.org/10.1021/acsomega.3c00306
20. Hongwei Lei, David Hardy and Feng Gao. Lead-free double perovskite Cs2AgBiBr6: Fundamentals, applications, and perspectives. Advanced Functional Materials 31 (2021): 2105898. https://doi.org/10.1002/adfm.202105898
21. Navdeep Kaur, Jaya Madan, Asaithambi Perumal and Rahul Pandey. Current matched all-perovskite tandem solar cells with low-lead perovskites achieving 31.9% efficiency and enhanced stability. Scientific Reports 15 (2025): 29724. https://doi.org/10.1038/s41598-025-99575-8
22. Shubhanshu Agarwal, Kiruba Catherine Vincent and Rakesh Agrawal. From synthesis to application: A review of BaZrS3 chalcogenide perovskites for optoelectronic devices. Nanoscale 17 (2025): 4250–4300. https://doi.org/10.1039/D4NR03880K
23. Md Habibur Rahman and Arun Mannodi-Kanakkithodi. Data-driven discovery of novel chalcogenide semiconductors for solar absorption. EES Solar Advance article (2026): —. https://doi.org/10.1039/D6EL00026F
24. Kumar Neupane, Sagar Bhattarai, Nitumoni Deka, Ahmet Sait Alali, Abderrahim Yousfi, Okba Saidani, Md. Ferdous Rahman, Abhinav Kumar and Hanen Karamti. Exclusive optimization of Cs2AgBi0.75Sb0.25Br6-based solar cells through device simulation. Multiscale and Multidisciplinary Modeling, Experiments and Design 8 (2025): 390. https://doi.org/10.1007/s41939-025-00985-y
25. Bowen Liang, Lulu Chen, Xingchao Shao, Xinye Yuan, Shen Yu, Wei Tang, Siyuan Zhu, Jie Zhang, Yan Jiang, Chunlei Yang and Weimin Li. Quasi-flat narrow-bandgap CIGS bottom cell for efficient perovskite/CIGS tandem photovoltaics. Energy Material Advances 5 (2024): 0127. https://doi.org/10.34133/energymatadv.0127